Check for updates

ADVANCED MATERIALS TECHNOLOGIES
www.advmattechnol.de

Radio Frequency Sensing-Based In Situ Temperature Measurements during Magnetic Resonance Imaging Interventional Procedures

*Mehmet Berk Bilgin, Mehmet Efe Tiryaki, Jelena Lazovic, and Metin Sitti**

Magnetic resonance imaging (MRI)-tuned radio-frequency (RF) sensors are used as a radiation-free alternative for tracking minimally invasive medical tool positions. However, in situ temperature sensing capabilities of the MRI-tuned RF sensors have not been thoroughly investigated yet. A self-resonating RF sensor capable of remote in situ temperature sensing during real-time interventional MRI is presented. The proposed RF sensor design relies on the temperature-dependent permittivity to tune or detune the resonant frequency. The sensor is tuned to match the resonant frequency of a 7 Tesla MRI (298 MHz) at body temperature, enabling a hyperintense signal in MR images. As temperature increases, the sensor detunes due to the change in the relative permittivity, and the hyperintense signal disappears in the MR image, serving as a direct visual indicator of the temperature change in real-time. In addition, the localized signal can be used for 3D position tracking of interventional medical devices. Using a 7 Tesla preclinical MRI, in vitro characterization and ex vivo feasibility of the proposed temperature sensing method are demonstrated in the clinically relevant temperature range of 36–42 °C with an accuracy of ±0.6 °C. Such RF sensors can provide safer operations in future MRI interventional procedures.

1. Introduction

Recently, magnetic resonance imaging (MRI)-guided minimally invasive interventional procedures have attracted extensive attention in the medical robotics as a potential alternative to traditional 2D fluoroscopic imaging methods with the MRI's ionizing-radiation-free nature and 3D high-resolution soft tissue imaging capabilities.[1–6] By developing different MRI-based medical robot or device designs, such as MRI-compatible guide wires,[7,8] soft pneumatic actuators,[9,10] piezo actuators,[11,12] focused ultrasound (FUS) systems,[5,13,14] active catheters,[15,16] needle insertion systems,[4,17,18] and magnetic microrobots[19–25] and millirobots,[26–29] researchers have demonstrated promising interventional procedures, such as laser ablation,[30–34] local hyperthermia,[14,35,36] and FUS ablation.[13,34,37] The usage of MRI is mainly limited to the position tracking and the steering control of such medical robots or devices with fiducial markers based on radiofrequency (RF) markers,[3,38–42] magnetic markers,[43–45] and contrast agents.[46–48]

One of the key challenges during many interventional MRI procedures is the risks associated with overheating, which threatens the safety of the patients. Numerous reports have been published concerning the heating of metallic components during the MR imaging;[49–65] therefore, a continuous in situ temperature monitoring is required for safe interventional MRI applications. MRI thermometry has been developed as an in situ temperature monitoring method.[66–69] Researchers have used MRI thermometry-based temperature feedback to control FUS hyperthermia operations[35,36,70] or to evaluate MRI-guided laser ablation therapies[6,31,71] and MRI-guided active catheters.[72,73] While MRI thermometry methods can provide accurate in situ temperature mapping in 3D, they decrease the overall MRI-based visual feedback rate by adding an extra sequence, hindering the real-time MRI feedback. In a different approach, some researchers have proposed RF-based telemetric devices for measuring the in situ temperature remotely.[74–78] However, such methods have included sophisticated circuitries and metallic components that may distort MR images.[79–81] Therefore, a safe method for in situ temperature monitoring without decreasing the MRI feedback rate is highly desirable inside the interventional MR scanners.

Previously, various RF marker designs have been reported; however, their main focus has been on device 3D tracking inside MRI.[3,38–42] Recent studies explored new designs for ensuring functionality independent of the marker orientation.[82–84] Beyond tracking, a recent study used an RF marker design

M. B. Bilgin, M. Sitti
College of Engineering
Koç University
Istanbul 34450, Turkey
E-mail: sitti@is.mpg.de
M. B. Bilgin, M. E. Tiryaki, M. Sitti
Physical Intelligence Department
Max Planck Institute for Intelligent Systems
70569 Stuttgart, Germany
M. E. Tiryaki, M. Sitti
Institute for Biomedical Engineering
ETH Zurich
Zurich 8092, Switzerland
J. Lazovic
Medical Systems Central Scientific Facility
Max Planck Institute for Intelligent Systems
70569 Stuttgart, Germany
The ORCID identification number(s) for the author(s) of this article can be found under https://doi.org/10.1002/admt.202101625.

© 2022 The Authors. Advanced Materials Technologies published by Wiley-VCH GmbH. This is an open access article under the terms of the Creative Commons Attribution License, which permits use, distribution and reproduction in any medium, provided the original work is properly cited.

DOI: 10.1002/admt.202101625

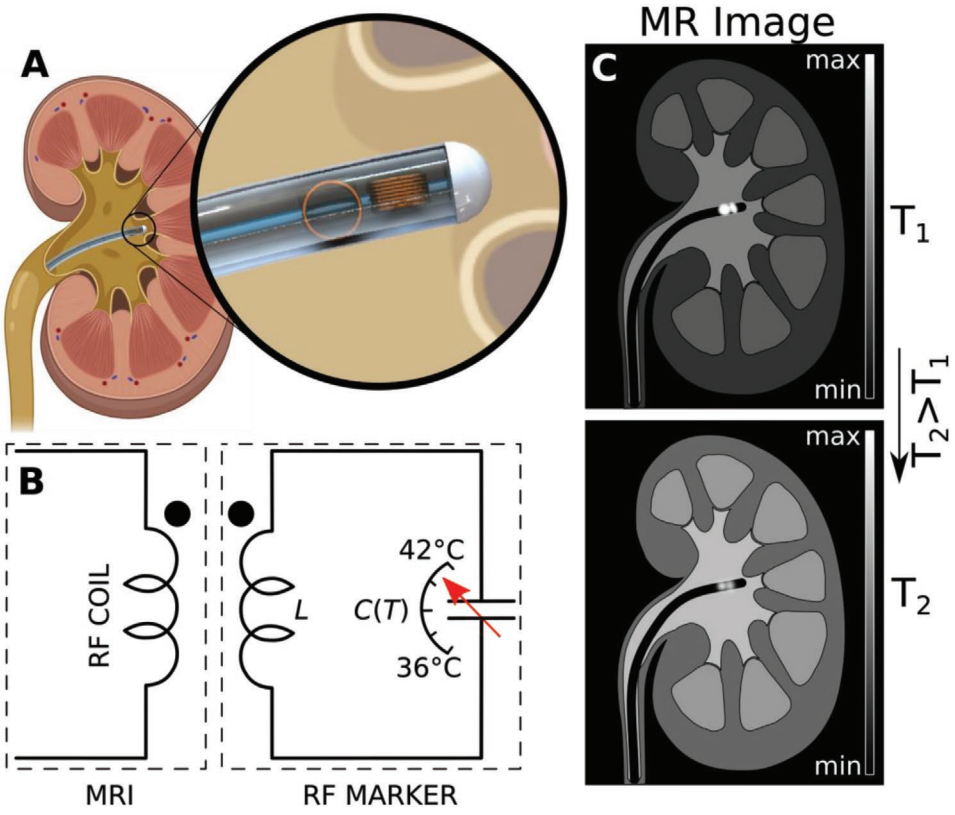


Figure 1. MRI-tuned RF resonator-based remote in situ temperature measurement inside an MRI. A) Schematic of the RF sensor with two coils integrated to the tip of a catheter. B) RF sensor circuit coupled with the MRI's RF coils. The intrinsic capacitance varies with temperature due to the temperature-dependent permittivity of water. C) Conceptual MRI images of the RF sensor in a kidney for two different temperatures. As the temperature rises, the sensor detunes and losses its high signal relative to the background image.

for remote bio-sensing in neuron transmission by using an additional field-effect transistor to detune the marker with the environmental stimulus.[85] An alternative approach for remote sensing is to leverage changes in the intrinsic parameters of the RF markers, such as inductance and capacitance. Hence, when a marker reacts to a stimulus, its resonant frequency shifts. With such a response mechanism, markers can be used as remote sensors and respond to stimuli while retaining their 3D position tracking abilities.

Here, we propose a 7 Tesla MRI-tuned RF sensor for remote temperature sensing (**Figure 1**A). Our RF sensor design is composed of two coils tuned to the operating frequency of the MRI scanner using the self-resonance of the copper wire wound into a solenoid coil. We place our sensor inside a dielectric material, a low-concentration agarose gel, where its resonant frequency can be changed with temperature due to the temperature dependence of permittivity. Temperature increase alters the permittivity and decreases the capacitance, thus, detunes the RF sensor (Figure 1B). Therefore, the signal intensity within the RF sensor in the MR image changes with temperature. We place two perpendicular RF markers and fill them with low concentration agarose gel to assure orientation independence during the excitation with the MRI RF coils. We provide further characterization of the RF sensor, such as the angle limit between the sensor and the MR imaging slice and the image resolution limit. For the ideal results, the marker should be oriented with the slice, and the image resolution should be lower than a limit determined by the marker size. The local in situ temperature is estimated from the MRI images using the calculated contrast between the RF marker and the surrounding tissue (Figure 1C). Our ex vivo temperature measurement experiments in a porcine heart tissue demonstrate that the proposed RF temperature marker has high precision in the operating temperature range of 36–42 °C. Therefore, it is possible to map absolute temperature values with precalibration of the signal with a known temperature.

2. Results

2.1. MRI-Tuned RF Marker Design for Remote In Situ Temperature Sensing

Previous research on MRI-tuned RF markers was focused only on the 3D localization and position tracking for MRI-guided medical tools[3–6,38–42,85–90] (see Table S1, Supporting Information). Therefore, the main design objective of these studies was to maximize the coupling between the RF marker and MRI's own RF coils by precisely tuning the marker to the operation frequency of the MRI scanner, ensuring RF coupling robustness against any external physical stimuli. However, using RF markers for remote sensing requires a different design

© 2022 The Authors. Advanced Materials Technologies published by Wiley-VCH GmbH

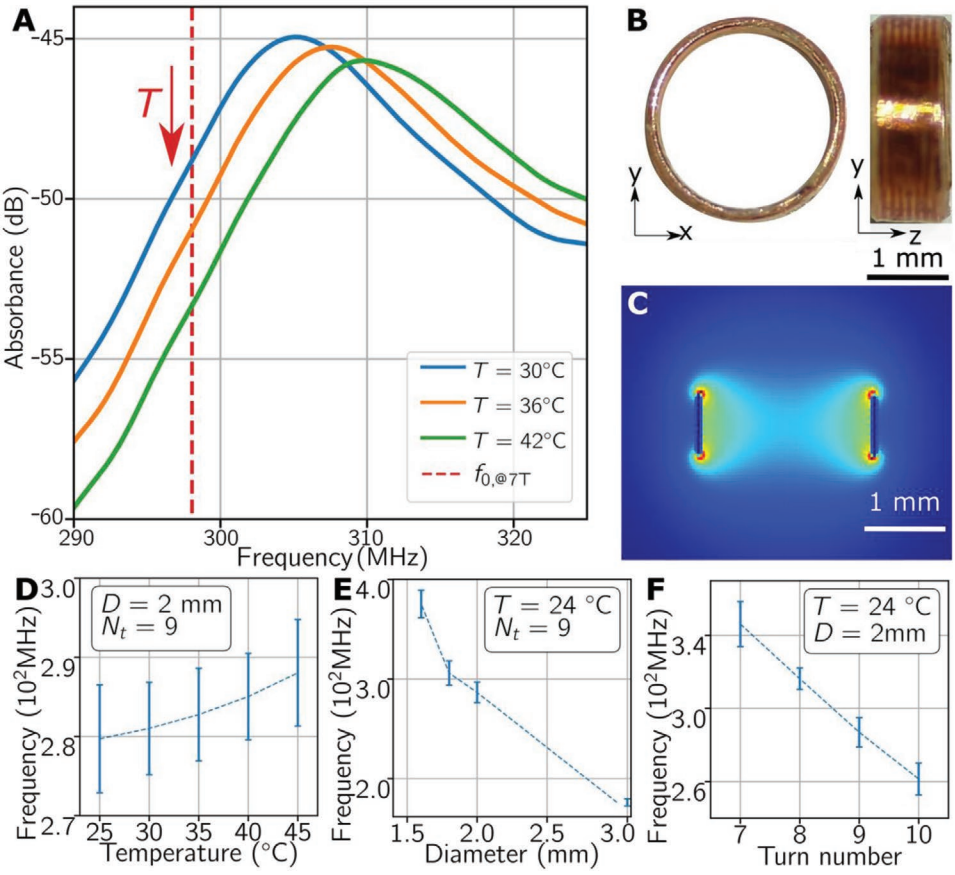


Figure 2. Tuning of the RF sensor for remote temperature sensing. A) The absorbance of a tuned coil in three different temperatures measured via a vector network analyzer. The red-colored dashed line shows the desired tuning for a linear temperature sensing. B) Top and side view photos of a prototype RF marker. C) COMSOL simulation of the electromagnetic field distribution in the RF sensor shown in (B). D–F) The experimentally measured resonant frequency of the RF sensor as a function of coil turn number (N_t), diameter (D), and temperature (T) while the other two are kept constant.

approach. The coupling between the RF markers and the MRI RF coils should be sensitive to the measured physical stimulus, as shown for our temperature markers in **Figure 2**A. We achieved a temperature-sensitive RF sensing by excluding the lumped capacitor element from the marker design and using solely the intrinsic capacitance (C_i) of our single-layer wound coil (Figure 2B) to match the resonance frequency, $f_0 = \frac{1}{2\pi\sqrt{LC_i}}$, where L is the inductance of the coil. The intrinsic capacitance is related to the coil geometry and proportional to the permittivity of the surrounding medium. For our single-layer-wound coil design, most B_1 field amplification occurred inside the coil (Figure 2C), therefore, it was placed inside a 1% agarose gel. Water-rich agarose gel provided a high density of ^{1}H protons for the MR imaging. Moreover, high water content also provided a dynamic response range for temperature measurement due to large variation in relative permittivity of water, around 0.35 °C^{-1} between 20 and 40 °C.[91,92]

Using only intrinsic capacitance is also advantageous in maximizing the quality factor of the markers and the RF coupling between the marker and the MRI's RF coils. The quality factor is directly proportional to the inductance and inversely proportional to the capacitance;[3] hence, the intrinsic capacitance-based design allows us to use the maximum possible quality factor for the desired resonance frequency f_0. Similarly, the RF coupling is a function of the mutual and self-inductances of marker and MRI RF coils.[83] Therefore, using intrinsic capacitance allows us to maximize mutual inductance and self-inductance, leading to a higher signal. However, tuning RF markers with intrinsic capacitance is much more demanding than simple LC circuit tuning since both inductance and capacitance depend on the geometric properties of the coil, i.e., its diameter and turn number. So, a tuning method with geometric manipulation has to be very precise.

We used a heuristic approach to tune our coils for remote temperature sensing. The first tuning step was to choose the resonant frequency region in which our coils operated. As shown in Figure 2A, the main goal was to tune the resonant frequency such that the coupling decreased linearly as the temperature increases in the operational temperature range of 36–42 °C. Thus, the marker gave a high-intensity MRI signal at lower temperatures and gradually lost signal strength with the temperature increase. This response was achieved by tuning the marker to the operating frequency of the MRI scanner (298 MHz for our 7 Tesla MRI) at room temperature 25 °C. When it reached the body temperature of 36 °C, resonant frequency shifted to higher frequencies. It is important to note that another linear response region could also be achieved by

© 2022 The Authors. Advanced Materials Technologies published by Wiley-VCH GmbH

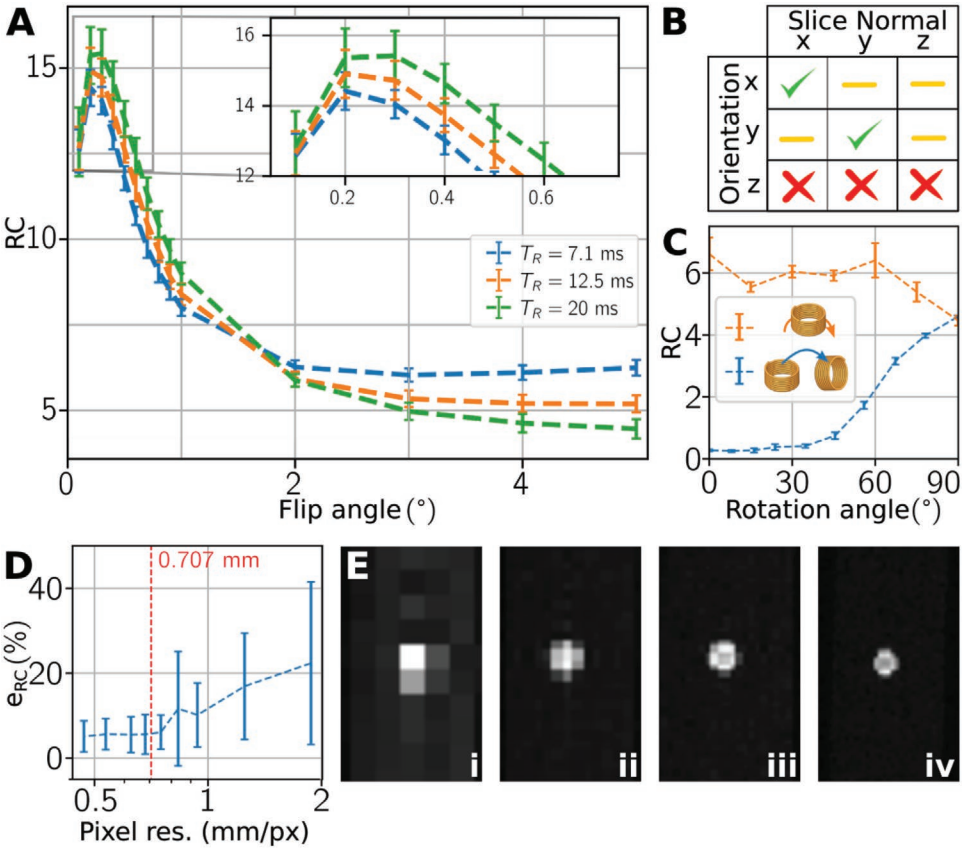


Figure 3. Characterization of the RF sensor inside a 7 Tesla preclinical MRI scanner. A) Relative contrast (RC) as a function of the MR flip angle with different repetition time values. B) Preferred marker and slice orientation combinations. C) RC values of the sensor with different angles (orange for rotation around *y*-axis and blue for rotation around *x*-axis). D) Deviation of the RC values in different MR imaging resolutions. E) MR image of a sensor in different resolutions. The resolutions of i–iv areas are 1.875, 0.750, 0.469, and 0.234 mm pixel^{-1}, respectively.

tuning the marker around 20 MHz less than the MRI's operating frequency at the body temperature. However, this would result in the temperature marker becoming visible only at high temperatures.

Next, the effects of the coil diameter, turn number, and ambient temperature (Figure 2D–F) on the resonant frequency were examined using a vector network analyzer (VNA). The final marker design in the desired temperature-dependent frequency regime was determined using the VNA characterization results. In the rest of the study, we used coils of 2 mm diameter with 8.5 to 9 turns of winding. Each marker was individually tuned to the Larmor frequency of ^{1}H at 7 T at room temperature. A similar heuristic method can also be followed to tune markers for lower field MRI scanners; however, the final diameter and turn number would be much higher to match the Larmor frequency. The best way to keep dimensions small would be winding onto the second and third layers of coils for lower resonance frequencies.

2.2. MR Imaging of the RF Markers

In MR imaging, the spin excitation is proportional to the transmitted RF magnetic field (B_{1+}). Flip angle (α) is a linear function of the gyromagnetic ratio (γ), the magnitude of the RF magnetic field (B_1), and the RF pulse duration (t_p) for small flip angles, where $\alpha = \gamma B_1 t_p$. Since RF markers amplify the local B_1 field, it increases the effective flip angle exciting the local spins. Therefore, we can take advantage of the locally amplified B_1 to obtain a positive contrast between the RF sensor and tissue by imaging with very low flip angles.[86] This study utilizes created contrast difference to measure temperature using a metric for relative contrast (RC), the ratio of the maximum signal intensity from the RF sensor to the mean background signal.

The first step of the characterization is to determine the optimum applied flip angle for imaging RF markers. RF markers were submerged in deionized water, and a gradient-recalled echo (GRE) sequence was performed with different flip angles and repetition times. The repetition time of the sequence directly affects the RC curve and the optimal flip angle value. The RC of different flip angles with different repetition times is shown in **Figure 3**A. Longer repetition times provided higher RC but made sequences longer as well. To maximize the RC and minimize the sequence duration, we used a 0.2° flip angle and a minimum repetition time of 7.1 ms in the rest of the experiments. We also observed that as flip angles converged to 5°, RC was decreased as low as 4, at which the anatomical image could be seen. This observation suggests that the same MRI sequence can be used for imaging only markers at low flip angles and tissue at higher flip angles. Lastly, in flip angle

© 2022 The Authors. Advanced Materials Technologies published by Wiley-VCH GmbH

Table 1. Required MR image resolutions and durations for the RF sensors with different coil diameters.

Diameter [mm]	Resolution [mm pixel^{-1}]	Sequence duration [ms]
1.6	0.565	1336
1.8	0.636	1104
2	0.707	928
3	1.060	495

characterization experiments, RF markers were tested at a 90° flip angle, the highest RF excitation pulse used in imaging, with the proposed imaging sequence to check any potential heating issues by placing a fiber optic temperature probe next to the marker. No RF marker-induced Joule heating was observed since B_1 amplification occurred on the agarose gel with virtually no ionic content.

The marker and imaging slice orientation is the second factor affecting the marker signal. MRI's quadrature volume coil creates two circularly polarized RF waves in the x–y plane; therefore, markers should be oriented with the x-axis or y-axis for maximum signal amplification. On the other hand, any marker facing the z-axis, i.e., B_0 field, has no coupling with the MRI RF coils; hence, it does not create signal amplification. In addition to the RF coupling, the relative orientation of the RF marker to the MR imaging slice also affects the signal. 2D MR images are composed of projection of the volumetric signal in slice to the 2D slice plane. Since the B_1 amplification pattern of our coils was not uniform, as shown in Figure 2C, a higher signal was observed when the coil was facing the same direction with the MRI slice than when the coil was perpendicular to the MRI slice.

Figure 3B gives a simple rule of thumb for combinations of the marker and slice orientations. While Figure 3B summarizes the geometric effects in cardinal directions, the marker signal in other orientations is also necessary to use the markers in realistic procedures. Therefore, the orientations were examined with a custom motorized rotating stage. While keeping the image slice fixed, y-axis-oriented marker was first rotated around y-axis using the motorized stage and then around x-axis manually. In the end, the marker was oriented facing the z-axis, i.e., the B_0 field. RC values of the marker during these rotations are reported in Figure 3C, as the first and second rotations appear as orange and blue colors, respectively. While the marker could keep the RC when rotated around the y-axis, the signal disappeared completely during rotation around the x-axis. In light of these experiments, two perpendicularly placed markers were selected as the final design for temperature monitoring experiments to ensure signal presence in every orientation.

Another important factor for the marker imaging is the spatial resolution. The marker shape in the MR images may vary depending on the relative position of the marker to the pixel grid due to the in-pixel signal averaging. However, the obtained RC should be consistent and fluctuate minimally between images to ensure reliable measurements. Therefore, the resolution should be decreased until stable RC measurements are achieved, and minimal fluctuation is ensured. To characterize the resolution limit, we imaged five markers with seven different slice positions and different image resolutions between 0.47 and 1.87 mm pixel^{-1}. Then, the mean and standard deviation of RC values were calculated. We observe that the RC variations (e_{RC}) were stabilized below 0.707 mm resolution for the 2 mm diameter markers, as shown in Figure 3D, and the mean RC value converged to a steady-state value (see Figure S1, Supporting Information). This limit essentially suggests that at least one full pixel projection of the image should be positioned inside the marker to minimize the RC variation (see Note S1, Supporting Information). MR images of the marker with different resolutions are provided in Figure 3E. B_1 field distribution is visible through the signal in images, verifies the simulations in Figure 2C. Pixel limits for markers in varying diameters with fixed turns for 298 MHz resonant frequency and their imaging sequence duration are provided in **Table 1**. The table shows a direct trade-off between the resolution and the imaging speed; hence, the MRI's spatiotemporal imaging resolution is a limiting factor.

To demonstrate the orientation-independent operation of our marker, we performed ex vivo experiments in a porcine kidney. RF sensor was attached to a commercial catheter tubing, and the catheter was steered manually inside MRI while imaging. Video snapshots with different orientations are shown in **Figure 4** and Movie S1 in the Supporting Information. RF sensors could be visualized in various orientations during the catheter navigation in the kidney. While the RF sensor signal could guide a catheter tip, it is important to note that it is not possible to monitor the temperature during the motion due to the motion artifacts as can be seen in Movie S1 in the Supporting Information.

2.3. Ex Vivo Temperature Measurements inside MRI

A mapping curve must be set before starting the ex vivo temperature measurements. Raw MRI signals cannot be used for direct measurement since they are tissue sensitive and prone to background interference. Therefore, RF markers tuned to linear temperature response regime at 298 MHz were placed in water baths with different thicknesses, and an optical temperature probe was placed next to the RF marker to measure reference temperature. First, the RF coil of the MRI scanner was tuned to the signal from 40 °C to have high RF coupling with water between 30 and 50 °C. Then, the water was heated to 50 °C. The samples were continuously imaged using the GRE sequence t_E/t_R = 3.438/7.183 ms with 0.2° flip angle during convective cooling of water. Since the relative permittivity of water is temperature dependent,[91,92] marker signals change with temperature. The temperature response of the markers is presented in Movie S2 in the Supporting Information with a color-coding. We observed in Movie S2 in the Supporting Information that the shape of the marker signal might change slightly depending on the relative position of the marker to the pixel. **Figure 5**A shows the statistical analysis of the RC values of five markers as a function of temperature for different slice thicknesses. It can be observed that created RC is inversely proportional to the thickness of the background water, but the relation is nonlinear. This is due to the signal integration characteristic of the MR slice imaging since 2D GRE sequences were used for this experiment. Moreover,

© 2022 The Authors. Advanced Materials Technologies published by Wiley-VCH GmbH

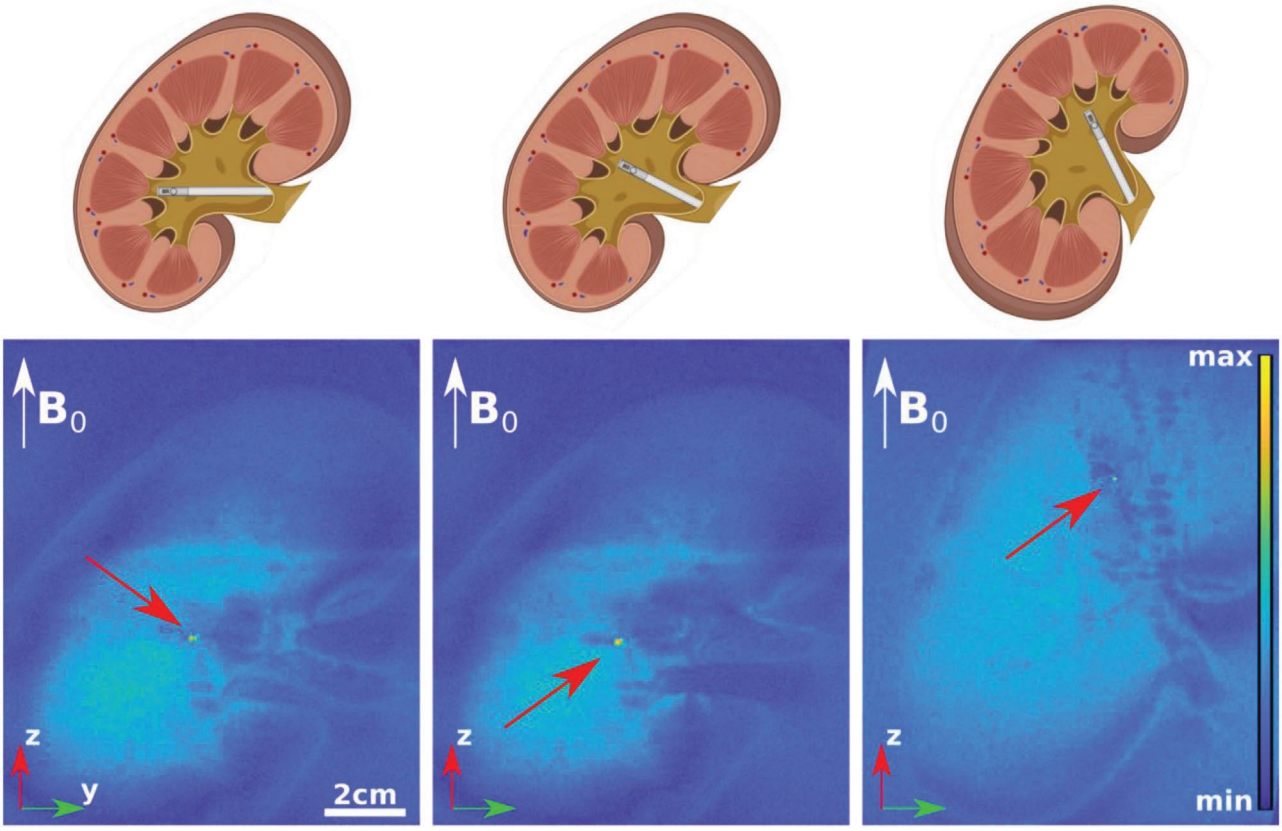


Figure 4. Experimental demonstration of the RF sensor, integrated on a manually operated catheter tip, in different orientations inside an ex vivo porcine kidney. A catheter with the integrated RF sensor was manually steered with the help of an extension inside the MRI while continuously imaging. The top figure illustrates the orientation of the catheter in the corresponding below MRI images. The hyperintense MRI yellow signal (shown by the red arrows) shows the position of the RF sensor on the catheter tip inside the kidney. The colorbar shows the maximum and minimum MRI signal levels.

while the temperature dependence of RC is relatively linear, around 40 °C, nonlinearity in lower and higher temperatures due to the detuning of the MRI scanner's RF coils was observed. However, since the temperatures are expected to be 36–42 °C during medical procedures to avoid tissue damage, this nonlinearity is not important in clinical applications.

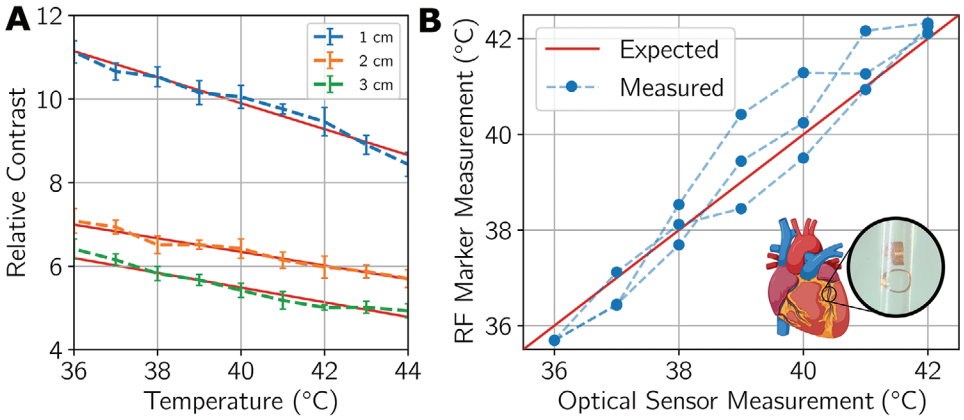


Figure 5. RF sensor-based temperature estimation inside an ex vivo porcine heart tissue. A) RC values of the RF sensors with different water thicknesses (1, 2, and 3 cm), where the temperatures were measured by the optical probe as the ground truth. RC value of each temperature is mean of 25 datapoints, and error bars represent their standard deviation. Red lines are the fitted line on mean RC values. B) Ex vivo temperature measurements results inside the heart tissue. Such measured temperatures were computed based on the fitted line ($R^2 = 0.979$) from the 1 cm thick water RC measurement in (A). The ex vivo heart tissue experiment was repeated with three different hearts, data from each experiment are given in (B) with connected points. The blue data points represent the computed ex vivo temperature values inside the heart tissue, and the red line does the ground truth values. The temperature measurements were conducted in the left diagonal artery of the heart with the two-coil RF sensor enclosed inside a tube with 1% agarose gel.

© 2022 The Authors. Advanced Materials Technologies published by Wiley-VCH GmbH

The MRI relaxation values of the actual tissue are different from water; therefore, we needed an additional mapping measurement to estimate the temperature. A linear line was fitted to the mapping data from Figure 5A to estimate the temperature with ex vivo experiment RC values. Since relaxation values were not changing significantly for our marker and tissue with temperature, we introduced a scaled RC, $RC^*(T) = RC_{water@36\ °C} \cdot RC_{tissue}(T)/RC_{tissue@36\ °C}$, using an initial calibration measurement obtained at 36 °C from the tissue. Finally, we obtained the following linear estimation, $T_{est} = c_1 RC^* + c_2$, where c_1 and c_2 are the line parameters fitted to data from the corresponding water thickness.

Porcine heart tissue was used to perform the ex vivo temperature measurement experiments. First, 10 mm thick heart tissue was cut to be 50–80 mm^2 rectangular shape. Next, the RF temperature marker made of two RF markers in a catheter tube was placed inside the artery, as shown in Figure 5B. An optical temperature probe was also placed near the RF marker to measure the reference temperatures. Next, the tissue was placed in a sample box thermally insulated with styrofoam. The tissue was heated by hot water circulation through the tubing at the bottom of the sample box and the calibration RC, $RC_{tissue@36\ °C}$, was recorded at $T = 36$ °C. Then, the temperature was estimated by imaging the tissue approximately every 2 min or so (see Figure S2, Supporting Information). The temperature estimation experiment was repeated three times, and the mean square root (RMS) error in these experiments was calculated around ± 0.6 °C for three experiments.

3. Discussion

This study demonstrates a remote in situ temperature measurement method based on an RF-resonator tuned to MRI's RF resonance frequency. We used a heuristic RF marker tuning approach to tune the markers to the operation frequency of our 7 Tesla MRI scanner (298 MHz). The proposed coil design is smaller than previous designs (see Table S1, Supporting Information) and the sensor is packaged and insulated in a nonionic gel medium to prevent unintentional temperature rise. The presented RF sensor could be used as a remote in situ temperature probe and position-tracking marker for interventional medical tools, such as a catheter. We demonstrate a temperature measurement precision comparable to the MRI thermometry sequences.[66–68] In contrast to MRI thermometry methods, we measure the temperature using a basic GRE-based MR imaging sequence and eliminating the need for alternating between anatomical and thermometric MRI images. Therefore, the proposed method can measure the temperature continuously with a refresh rate less than 1.8 s, which is 10–30 times faster than the standard thermometric sequences used in the literature,[6,68] and ≈2 times faster than the echo-planar imaging-based fast thermometry methods.[66,73]

Such fast temperature feedback would benefit the interventional MRI procedures and laser ablation procedures inside an MR scanner. During the interventional MRI applications, patients' body should be imaged continuously to guide interventional tools toward the target locations. However, continuous imaging of the tissue could cause a temperature rise. The proposed RF temperature sensors can allow the surgeon to monitor the tissue temperature continuously and safely guide the interventional tool for a longer period of time. Moreover, the fast temperature feedback can enable a precise control over the thermal dose during laser ablation operations[6] and can provide safer operation by fast monitoring of the laser tip temperature to avoid unintentional local ablation around the surgical tool. Lastly, the temperature rise is also a major issue in electromagnetically actuated steerable MRI catheter tips.[93,94] The temperature sensors can also be employed in the proximity of the steering coil to monitor the catheter tip temperature during the catheter actuation and help to regulate currents accordingly to prevent any tissue heating.

However, integrating the RF sensor to dynamically actuated interventional tools would be challenging. The proposed temperature measurement is limited to stationary conditions, i.e., when the sensor does not move. The motion would create undesirable artifacts in the MR image reconstruction and hinder a precise measurement. Therefore, it is not possible to monitor the temperature and track the marker position simultaneously, at this stage. However, in the future, motion correction and sparse reconstruction methods could be used to monitor the temperature and the position simultaneously for moving RF markers.[95–97] In vivo conditions also have similar motion challenges, such as peristaltic organ motions, breathing, and heart beatings. In future studies, cine imaging[98] can be employed for temperature measurements near a beating heart. Another limitation of the presented work is the use of a 7 Tesla preclinical MRI scanner. While 7 Tesla MRI scanners start to be a part of the clinical environment,[99] most of the clinical MRI scanners are 1.5 and 3 Tesla. To adapt the proposed RF sensor to 1.5 and 3 Tesla scanners, resonance frequency of the coil should be tuned to 63.9 and 127.8 MHz, respectively. A similar heuristic method can be followed to tune markers for lower-field MRI scanners. Considering the resonance frequency trends in Figure 2E,F, either diameter or turn number should be increased to match the corresponding Larmor frequencies. Since the marker diameter is critical for fitting the RF sensor to minimally invasive medical tools, the turn number should be increased by winding onto the second and third layers of the coils for lower resonance frequencies.

Furthermore, besides the temperature, other biological stimuli could also be measured in a similar strategy of leveraging environment-dependent intrinsic parameters of the RF markers, which is a future work. Many other stimuli, such as ionic content, ion concentrations,[100] and physical deformations,[101] can be employed for this sensory response. Hai et al. demonstrated that a similar system could be used in biological investigations.[85] Body fluids and tissues have varying permittivity[102,103] and, when markers are designed to be selectively responsive, this could be used as a flag mechanism for tissue selection. Also, markers sensitive to other stimuli would make catheter operations more functional. Thus, the proposed RF marker-based remote MRI sensing could be an integral part of future MRI-guided active catheters[16,50,104–106] and endoscopic tools[13,107–109] and provide safer medical operations.

4. Experimental Section

Design and Manufacturing of the RF Marker: MRI RF markers were manufactured by winding an 80 µm diameter insulated copper wire

© 2022 The Authors. Advanced Materials Technologies published by Wiley-VCH GmbH

(Block, Germany) to a 14G hypodermic needle (Henke-Ject, Henke Sass Wolf GmbH, Germany). A layer of glue (Loctite 401, Henkel, Germany) was applied, and after drying, individual markers were cut (see Figure S3, Supporting Information). Markers were trimmed and tuned one by one, using a VNA (ENA20561B, Keysight Technologies, CA, USA). Using a coil loop attached to the VNA in the S11 mode, tuning measurements were done as markers were submerged in water. The magnetic field pattern of the coil was also simulated in the COMSOL environment using a simplified axially symmetric electromagnetic module to understand the distribution of the effective applied magnetic field. A polyurethane catheter tube (Pellethane, Lubrizol, OH, USA) with a 2.8 mm diameter was used for temperature measurement experiments. Two markers were placed perpendicularly inside the catheter tube, filled, and mechanically fixed with a low concentration agarose gel (Agarose, Sigma-Aldrich, MO, USA). The ends of the catheter tube were sealed to prevent the Ringer's solution from diffusing into the agarose and detuning the sensor.

MRI Hardware and Experimental Setup: 7 Tesla preclinical small animal MRI (BioSpec 70/30, Bruker, Ettlingen, Germany) and 154 mm quadrature birdcage coil were used for MRI experiments. A custom MRI-compatible horizontal rotating table was designed for sensor rotation experiments inside the MR scanner. The nonmagnetic piezo motor and wires were kept outside the bore of the MRI to minimize any RF interference with MRI. A pulley attached to a piezo motor (LR23-50, PiezoMotor, Sweden), stationed at the MRI bore entrance, rotated the table with the help of a tight string. The piezo motor was used for horizontal rotation to rotate the table in 10° intervals inside the MRI. However, vertical rotations were done manually in 15° intervals. In ex vivo experiments, a porcine heart tissue containing an artery was cut and placed in a sample box with polyvinyl tubing in a spiral pattern installed at the bottom for tissue heating experiments. The sample box was filled with Ringer's solution to increase heat transfer and placed in a styrofoam hold. A heated bath circulator (SC100-S5P, ThermoFisher Scientific, MA, United States) pumped hot water through the pipes that are installed in the sample box and heated the heart tissue. A Catheter with two perpendicular markers was placed in one of the arteries, and an optical temperature probe (FOTEMP OEM-PLUS, Optocon, Germany) was placed next to it. MRI scans were conducted as temperatures were measured with the optical sensor as the ground truth.

MRI Imaging and Data Evaluation: In MRI experiments, a 2D nonslice selective GRE sequence was used. A minimum echo time of 3.438 ms and a minimum repetition time of 7.183 ms were used. 120×120 mm^2 field of view was imaged with 256×256 pixel^2 matrix, if not stated otherwise. The single imaging sequence lasted around 1.8 s. 100 kHz excitation pulse bandwidth was used in all experiments, and the receiver coil bandwidth was set to 50 kHz. Pulse power was adjusted to have a flip angle of 0.2°. An automated software routine was created to evaluate the RC values of RF markers in pixel size and rotation angle experiments. The code detected the corners of the sample box, therefore, the orientation angle of the sample box, and rotated it to 90°. After the rotation correction, it identified each sample well and checked for markers. The signal of the water regions was used for background signals after removing markers from the image. Then the following formula was used for the calculation of the RC

$$RC = \frac{\max(marker) - mean(background)}{mean(background)} \quad (1)$$

In ex vivo experiments, marker positions and selected background regions were manually given to code, and the software RC values were calculated. Then, calculated RC values were converted to temperature estimations by the software using the mapping relation.

Statistical Analysis: All quantitative values were presented as the means ± standard deviation of the mean.

Supporting Information

Supporting Information is available from the Wiley Online Library or from the author.

Acknowledgements

The authors thank M. Phelan and C.B. Dayan for their help in manufacturing the coils and experimental setups. Figures 1 and 4 are created with the help of BioRender.com. This work was funded by the Max Planck Society.

Open access funding enabled and organized by Projekt DEAL.

Conflict of Interest

The authors declare no conflict of interest.

Author Contributions

M.B.B. and M.E.T. contributed equally to this work. M.B.B. and M.E.T. participated in the study design, MRI sequence development, RF sensor design fabrication, experimental procedures design, data collection, data analysis, and manuscript writing. J.L. participated in RF sensor design, MRI experiments, and manuscript writing. M.S. participated in the study design, discussions, supervision, and manuscript writing.

Data Availability Statement

The data that support the findings of this study are available in the supplementary material of this article.

Keywords

interventional MRI, MRI-guided devices, MRI thermometry, RF markers, temperature sensing

Received: December 8, 2021
Revised: February 17, 2022
Published online:

[1] Ö. Erin, M. Boyvat, M. E. Tiryaki, M. Phelan, M. Sitti, *Adv. Intell. Syst.* **2020**, *2*, 1900110.
[2] M. W. Wilson, A. B. Martin, P. Lillaney, A. D. Losey, E. J. Yee, A. Bernhardt, V. Malba, L. Evans, R. Sincic, M. Saeed, R. L. Arenson, S. W. Hetts, *J. Vasc. Interv. Radiol.* **2013**, *24*, 885.
[3] C.-L. Cheung, J. D.-L. Ho, V. Vardhanabhuti, H.-C. Chang, K.-W. Kwok, *IEEE/ASME Trans. Mechatron.* **2020**, *25*, 1016.
[4] Z. He, Z. Dong, G. Fang, J. D.-L. Ho, C.-L. Cheung, H.-C. Chang, C. C.-N. Chong, J. Y.-K. Chan, D. T. M. Chan, K.-W. Kwok, *IEEE Rob. Autom. Lett.* **2020**, *5*, 2100.
[5] J. Dai, Z. He, G. Fang, X. Wang, Y. Li, C.-L. Cheung, L. Liang, I. Iordachita, H.-C. Chang, K.-W. Kwok, *IEEE Rob. Autom. Lett.* **2021**, *6*, 5137.
[6] G. Fang, M. C. K. Chow, J. D. L. Ho, Z. He, K. Wang, T. C. Ng, J. K. H. Tsoi, P.-L. Chan, H.-C. Chang, D. T.-M. Chan, Y. H. Liu, F. C. Holsinger, J. Y. Chan, K. W. Kwok, *Sci. Rob.* **2021**, *6*, eabg5575.
[7] S. Krueger, S. Schmitz, S. Weiss, D. Wirtz, M. Linssen, H. Schade, N. Kraemer, E. Spuentrup, G. Krombach, A. Buecker, *Magn. Reson. Med.* **2008**, *60*, 1190.
[8] S. Kos, R. Huegli, E. Hofmann, H. H. Quick, H. Kuehl, S. Aker, G. M. Kaiser, P. J. A. Borm, A. L. Jacob, D. Bilecen, *Cardiovasc. Interv. Radiol.* **2009**, *32*, 514.
[9] Y. Wang, H. Su, K. Harrington, G. Fischer, in *Dynamic Systems And Control Conf.*, ASME, Cambrigde, MA, USA **2010**, pp. 23–28.

© 2022 The Authors. Advanced Materials Technologies published by Wiley-VCH GmbH

[10] W. Shang, H. Su, G. Li, G. S. Fischer, in *2013 IEEE/RSJ Int. Conf. Intelligent Robots and Systems* (Ed: S. Sugano), IEEE, Piscataway, NJ **2013**, pp. 4092–4098.
[11] H. Su, W. Shang, G. Cole, G. Li, K. Harrington, A. Camilo, J. Tokuda, C. M. Tempany, N. Hata, G. S. Fischer, *IEEE/ASME Trans. Mechatron.* **2015**, *20*, 1920.
[12] H. Su, D. C. Cardona, W. Shang, A. Camilo, G. A. Cole, D. C. Rucker, R. J. Webster, G. S. Fischer, in *Proc. – IEEE Int. Conf. Robotics and Automation* (Ed: N. Papanikolopoulos), IEEE, Piscataway, NJ **2012**, pp. 1939–1945.
[13] X. Liu, N. Ellens, E. Williams, E. C. Burdette, P. Karmarkar, C. R. Weiss, D. Kraitchman, P. A. Bottomley, *Magn. Reson. Med.* **2020**, *83*, 240.
[14] R. Staruch, R. Chopra, K. Hynynen, *Int. J. Hyperthermia* **2011**, *27*, 156.
[15] H. H. Quick, M. O. Zenge, H. Kuehl, G. Kaiser, S. Aker, S. Massing, S. Bosk, M. E. Ladd, *Magn. Reson. Med.* **2005**, *53*, 446.
[16] C. M. Hillenbrand, D. R. Elgort, E. Y. Wong, A. Reykowski, F. K. Wacker, J. S. Lewin, J. L. Duerk, *Magn. Reson. Med.* **2004**, *51*, 668.
[17] Y. Qiu, L. Wu, F. Huang, Z. Huang, Q. Yan, J. Guo, in *2021 6th IEEE Int. Conf. Advanced Robotics and Mechatronics (ICARM)*, (Ed: J. Luo), IEEE, Piscataway, NJ **2021**, pp. 86–92.
[18] K. Masamune, E. Kobayashi, Y. Masutani, M. Suzuki, T. Dohi, H. Iseki, K. Takakura, *J. Image Guided Surg.* **1995**, *1*, 242.
[19] M. Vonthron, V. Lalande, G. Bringout, C. Tremblay, S. Martel, in *2011 IEEE/RJS Int. Conf. Intelligent Robots and Systems* (Ed: N. M. Amato), IEEE, Piscataway, NJ **2011**, pp. 1285–1290.
[20] G. K'osa, P. Jakab, G. Sz'ekely, N. Hata, *Biomed. Microdevices* **2012**, *14*, 165.
[21] A. Aziz, S. Pane, V. Iacovacci, N. Koukourakis, J. Czarske, A. Menciassi, M. Medina-S'anchez, O. G. Schmidt, *ACS Nano* **2020**, *14*, 10865.
[22] J.-B. Mathieu, S. Martel, *Magn. Reson. Med.* **2010**, *63*, 1336.
[23] L. Arcese, M. Fruchard, A. Ferreira, in *2009 IEEE/RSJ Int. Conf. Intelligent Robots and Systems (IROS 2009)* (Ed: N. Xi), IEEE, Piscataway, NJ **2009**, pp. 534–539.
[24] L. Arcese, M. Fruchard, F. Beyeler, A. Ferreira, B. J. Nelson, in *Proc. – IEEE Int. Conf. Robotics and Automation* (Ed: Z. Li), IEEE, Piscataway, NJ **2011**, pp. 4121–4126.
[25] M. E. Tiryaki, M. Sitti, *Adv. Intell. Syst.* **2021**, 2100178.
[26] A. T. Becker, O. Felfoul, P. E. Dupont, in *Proc. – IEEE Int. Conf. Robotics and Automation* (Ed: L. Parker), IEEE, Piscataway, NJ **2015**, pp. 1184–1189.
[27] O. Erin, M. Boyvat, J. Lazovic, M. E. Tiryaki, M. Sitti, *Adv. Sci.* **2021**, *8*, 2100463.
[28] O. Erin, H. B. Gilbert, A. F. Tabak, M. Sitti, *IEEE Trans. Rob.* **2019**, *35*, 1323.
[29] S. Mutlu, O. Yasa, O. Erin, M. Sitti, *Adv. Sci.* **2021**, *8*, 2002948.
[30] K. Ahrar, R. J. Stafford, *Tech. Vasc. Interv. Radiol.* **2011**, *14*, 177.
[31] J. G. R. Bomers, E. B. Cornel, J. J. Fütterer, S. F. M. Jenniskens, H. E. Schaafsma, J. O. Barentsz, J. P. M. Sedelaar, C. A. Hulsbergen-van de Kaa, J. A. Witjes, *World J. Urol.* **2017**, *35*, 703.
[32] G. P. Zientara, P. Saiviroonporn, P. R. Morrison, M. P. Fried, S. G. Hushek, R. Kikinis, F. A. Jolesz, *J. Magn. Reson. Imaging* **1998**, *8*, 1306.
[33] Z. Tovar-Spinoza, D. Carter, D. Ferrone, Y. Eksioglu, S. Huckins, *Child's Nerv. Syst.* **2013**, *29*, 2089.
[34] Y. Chen, A. Squires, R. Seifabadi, S. Xu, H. K. Agarwal, M. Bernardo, P. A. Pinto, P. Choyke, B. Wood, Z. T. H. Tse, *IEEE/ASME Trans. Mechatron.* **2017**, *22*, 107.
[35] R. Salomir, F. C. Vimeux, J. A. De Zwart, N. Grenier, C. T. W. Moonen, *Magn. Reson. Med.* **2000**, *43*, 342.
[36] M. Tillander, S. Hokland, J. Koskela, H. Dam, N. P. Andersen, M. Pedersen, K. Tanderup, M. Ylihautala, M. Köhler, *Med. Phys.* **2016**, *43*, 1539.
[37] A. Antoniou, M. Giannakou, N. Evripidou, G. Evripidou, K. Spanoudes, G. Menikou, C. Damianou, *Int. J. Med. Rob. Comput. Assist. Surg.* **2021**, *17*, e2299.
[38] N. Garnov, G. Thörmer, R. Trampel, W. Gründer, T. Kahn, M. Moche, H. Busse, *Med. Phys.* **2011**, *38*, 6327.
[39] M. Rea, D. McRobbie, H. Elhawary, T. H. Zion, M. Lamperth, I. Young, *Magn. Reson. Mater. Phys., Biol. Med.* **2009**, *22*, 71.
[40] F. Galassi, D. Brujic, M. Rea, N. Lambert, N. Desouza, M. Ristic, *Magn. Reson. Mater. Phys., Biol. Med.* **2015**, *28*, 33.
[41] O. Nassar, D. Mager, J. G. Korvink, *IEEE J. Electromagn. RF Microwaves Med. Biol.* **2020**, *5*, 78.
[42] A. Alipour, S. Gokyar, O. Algin, E. Atalar, H. V. Demir, *Magn. Reson. Med.* **2018**, *80*, 361.
[43] K. Zhang, A. J. Krafft, R. Umathum, F. Maier, W. Semmler, M. Bock, *Magn. Reson. Mater. Phys., Biol. Med.* **2010**, *23*, 153.
[44] C. Dahmen, K. Belharet, D. Folio, A. Ferreira, S. Fatikow, *Int. J. Optomechatronics* **2016**, *10*, 73.
[45] M. E. Tiryaki, Ö. Erin, M. Sitti, *IEEE Rob. Autom. Lett.* **2020**, *5*, 4501.
[46] P. Magnusson, E. Johansson, S. Månsson, J. S. Petersson, C. M. Chai, G. Hansson, O. Axelsson, K. Golman, *Magn. Reson. Med.* **2007**, *57*, 1140.
[47] S. Kozerke, S. Hegde, T. Schaeffter, R. Lamerichs, R. Razavi, D. L. Hill, *Magn. Reson. Med.* **2004**, *52*, 693.
[48] N. Whiting, J. Hu, J. V. Shah, M. C. Cassidy, E. Cressman, N. Z. Millward, D. G. Menter, C. M. Marcus, P. K. Bhattacharya, *Sci. Rep.* **2015**, *5*, 12842.
[49] M. F. Dempsey, B. Condon, *Clin. Radiol.* **2001**, *56*, 457.
[50] R. C. Susil, C. J. Yeung, H. R. Halperin, A. C. Lardo, E. Atalar, *Magn. Reson. Med.* **2002**, *47*, 594.
[51] W. R. Nitz, A. Oppelt, W. Renz, C. Manke, M. Lenhart, J. Link, *J. Magn. Reson. Imaging* **2001**, *13*, 105.
[52] G. H. Griffin, K. J. T. Anderson, H. Celik, G. A. Wright, *Magn. Reson. Med.* **2015**, *73*, 427.
[53] S. M. Park, R. Kamondetdacha, J. A. Nyenhuis, *J. Magn. Reson. Imaging* **2007**, *26*, 1278.
[54] M. E. Ladd, H. H. Quick, *Magn. Reson. Med.* **2000**, *43*, 615.
[55] S. Wildermuth, C. L. Dumoulin, T. Pfammatter, S. E. Maier, E. Hofmann, J. F. Debatin, *Cardiovasc. Interv. Radiol.* **1998**, *21*, 404.
[56] F. Godinez, R. Tomi-Tricot, M. Delcey, S. E. Williams, R. Mooiweer, B. Quesson, R. Razavi, J. V. Hajnal, S. J. Malik, *Magn. Reson. Med.* **2021**, *86*, 3360.
[57] L. Winter, F. Seifert, L. Zilberti, M. Murbach, B. Ittermann, *J. Magn. Reson. Imaging* **2021**, *53*, 1646.
[58] G. Bashein, G. Syrovy, *Anesthesiology* **1991**, *75*, 382.
[59] M. K. Konings, L. W. Bartels, H. F. M. Smits, C. J. G. Bakker, *J. Magn. Reson. Imaging* **2000**, *12*, 79.
[60] I. Khodarahmi, L. W. Bonham, C. R. Weiss, J. Fritz, *Invest. Radiol.* **2020**, *55*, 396.
[61] R. Buchli, P. Boesiger, D. Meier, *Magn. Reson. Med.* **1988**, *7*, 255.
[62] J. A. Nyenhuis, S.-M. Park, R. Kamondetdacha, A. Amjad, F. G. Shellock, A. R. Rezai, *IEEE Trans. Device Mater. Reliab.* **2005**, *5*, 467.
[63] A. Boutet, C. T. Chow, K. Narang, G. J. B. Elias, C. Neudorfer, J. Germann, M. Ranjan, A. Loh, A. J. Martin, W. Kucharczyk, C. J. Steele, I. Hancu, A. R. Rezai, A. M. Lozano, *Radiology* **2020**, *296*, 250.
[64] L. Golestanirad, J. Kirsch, G. Bonmassar, S. Downs, B. Elahi, A. Martin, M.-I. Iacono, L. M. Angelone, B. Keil, L. L. Wald, J. Pilitsis, *Neuroimage* **2019**, *184*, 566.
[65] J. Haik, S. Daniel, A. Tessone, A. Orenstein, E. Winkler, *Burns* **2009**, *35*, 294.
[66] M. Delcey, P. Bour, V. Ozenne, W. Ben Hassen, B. Quesson, *PLoS One* **2021**, *16*, e0250636.

© 2022 The Authors. Advanced Materials Technologies published by Wiley-VCH GmbH

[67] T. Kahn, T. Harth, J. C. W. Kiwit, H.-J. Schwarzmaier, C. Wald, U. Mödder, *J. Magn. Reson. Imaging* **1998**, *8*, 160.
[68] J. De Poorter, C. De Wagter, Y. De Deene, C. Thomsen, F. Staahlberg, E. Achten, *Magn. Reson. Med.* **1995**, *33*, 74.
[69] V. Rieke, in *Interventional Magnetic Resonance Imaging* (Eds: T. Kahn, H. Busse), Springer, Berlin/Heidelberg, Germany **2011**, pp. 271–288.
[70] A. Vanne, K. Hynynen, *Phys. Med. Biol.* **2003**, *48*, 31.
[71] L. Chen, J. P. Wansapura, G. Heit, K. Butts, *J. Magn. Reson. Imaging* **2002**, *16*, 147.
[72] P. Wang, O. Unal, *J. Magn. Reson. Imaging* **2015**, *41*, 851.
[73] V. Ozenne, S. Toupin, P. Bour, B. D. de Senneville, M. Lepetit-Coiffé, M. Boissenin, J. Benois-Pineau, M. S. Hansen, S. J. Inati, A. Govari, P. Jaïs, B. Quesson, *Magn. Reson. Med.* **2017**, *77*, 673.
[74] M. A. Ertürk, A. M. M. El-Sharkawy, P. A. Bottomley, *Med. Phys.* **2015**, *42*, 1411.
[75] T. T. Thai, J. M. Mehdi, F. Chebila, H. Aubert, P. Pons, G. R. Dejean, M. M. Tentzeris, R. Plana, *IEEE Sens. J.* **2012**, *12*, 2756.
[76] A. E. M. M. El-Sharkawy, P. P. Sotiriadis, P. A. Bottomley, E. Atalar, *IEEE Trans. Circuits Syst. I: Regul. Pap.* **2006**, *53*, 2396.
[77] A. Vaz, A. Ubarretxena, I. Zalbide, D. Pardo, H. Solar, A. Garcia-Alonso, R. Berenguer, *IEEE Trans. Circuits Syst. II: Express Briefs* **2010**, *57*, 95.
[78] A. C. Özen, B. Silemek, T. Lottner, E. Atalar, M. Bock, *Magn. Reson. Med.* **2020**, *84*, 1048.
[79] D. Schröder, G. Grupe, G. Rademacher, S. Mutze, A. Ernst, R. Seidl, P. Mittmann, *Biomed Res. Int.* **2018**, *2018*, 9163285.
[80] A. S. Soliman, A. Owrangi, A. Ravi, W. Y. Song, *J. Contemp. Brachytherapy* **2016**, *4*, 363.
[81] B. A. Hargreaves, P. W. Worters, K. B. Pauly, J. M. Pauly, K. M. Koch, G. E. Gold, *Am. J. Roentgenol.* **2011**, *197*, 547.
[82] E. Baysoy, D. K. Yildirim, C. Ozsoy, S. Mutlu, O. Kocaturk, *Magn. Reson. Mater. Phys., Biol. Med.* **2017**, *30*, 93.
[83] O. Nassar, D. Mager, J. G. Korvink, *IEEE J. Electromagn. RF Microwaves Med. Biol.* **2021**, *5*, 78.
[84] C. D. Jordan, B. R. H. Thorne, A. Wadhwa, A. D. Losey, E. Ozhinsky, S. Kondapavulur, V. Fratello, T. Moore, C. Stillson, C. Yee, R. D. Watkins, G. C. Scott, A. J. Martin, X. Zhang, M. W. Wilson, S. W. Hetts, *IEEE Trans. Biomed. Eng.* **2019**, *67*, 876.
[85] A. Hai, V. C. Spanoudaki, B. B. Bartelle, A. Jasanoff, *Nat. Biomed. Eng.* **2019**, *3*, 69.
[86] M. Burl, G. A. Coutts, I. R. Young, *Magn. Reson. Med.* **1996**, *36*, 491.
[87] S. Weiss, T. Kuehne, F. Brinkert, G. Krombach, M. Katoh, T. Schaeffter, R. W. Guenther, A. Buecker, *Magn. Reson. Med.* **2004**, *52*, 860.
[88] T. Kuehne, R. Fahrig, K. Butts, *J. Magn. Reson. Imaging* **2003**, *17*, 620.
[89] D. Ellersiek, H. Fassbender, P. Bruners, J. G. Pfeffer, T. Penzkofer, A. H. Mahnken, T. Schmitz-Rode, W. Mokwa, U. Schnakenberg, *Sens. Actuators, B* **2010**, *144*, 432.
[90] K. Will, S. Schimpf, A. Brose, F. Fischbach, J. Ricke, B. Schmidt, G. Rose, *Proc. SPIE* **2010**, *7625*, 76251Z.
[91] C. G. Malmberg, A. A. Maryott, *J. Res. Natl. Bur. Stand. (1934).* **1956**, *56*, 1.
[92] W. J. Ellison, *J. Phys. Chem. Ref. Data* **2007**, *36*, 1.
[93] T. Liu, N. L. Poirot, D. Franson, N. Seiberlich, M. A. Griswold, M. C. Çavuşoğlu, *IEEE Trans. Biomed. Eng.* **2016**, *63*, 2142.
[94] S. W. Hetts, M. Saeed, A. J. Martin, L. Evans, A. F. Bernhardt, V. Malba, F. Settecase, L. Do, E. J. Yee, A. Losey, R. Sincic, P. Lillaney, S. Roy, R. L. Arenson, M. W. Wilson, *Am. J. Neuroradiol.* **2013**, *34*, 2083.
[95] H. Zimmermann, S. Zuehlsdorff, R. Umathum, S. Volz, W. Semmler, M. Bock, in *Proc. Int. Society for Magnetic Resonance in Medicine*, ISMRM, Toronto, Canada **2003**, p. 1059.
[96] A. S. C. Yang, M. Kretzler, S. Sudarski, V. Gulani, N. Seiberlich, *Invest. Radiol.* **2016**, *51*, 349.
[97] D. K. Sodickson, W. J. Manning, *Magn. Reson. Med.* **1997**, *38*, 591.
[98] A. D. Curtis, H. L. M. Cheng, *J. Magn. Reson. Imaging* **2020**, *55*, 373.
[99] O. Kraff, H. H. Quick, *J. Magn. Reson. Imaging* **2017**, *46*, 1573.
[100] S. K. Aggarwal, R. H. Johnston, *IETE Tech. Rev. (Inst. Electron. Telecommun. Eng. India)* **1988**, *5*, 317.
[101] S. Charkhabi, Y. J. Chan, D.-G. Hwang, S. T. Frey, M. D. Bartlett, N. F. Reuel, *Adv. Mater. Technol.* **2019**, *4*, 1800683.
[102] T. Voigt, U. Katscher, O. Doessel, *Magn. Reson. Med.* **2011**, *66*, 456.
[103] R. Pethig, *Clinical Physics and Physiological Measurements* **1987**, p. 8.
[104] Y. S. Yaras, D. K. Yildirim, D. A. Herzka, T. Rogers, A. E. Campbell-Washburn, R. J. Lederman, F. L. Degertekin, O. Kocaturk, *Magn. Reson. Med.* **2021**, *85*, 2904.
[105] J. M. Serfaty, X. Yang, P. Aksit, H. H. Quick, M. Solaiyappan, E. Atalar, *J. Magn. Reson. Imaging* **2000**, *12*, 590.
[106] J. A. Bell, C. E. Saikus, K. Ratnayaka, V. Wu, M. Sonmez, A. Z. Faranesh, J. H. Colyer, R. J. Lederman, O. Kocaturk, *J. Magn. Reson. Imaging* **2012**, *35*, 908.
[107] X. Liu, P. Karmarkar, D. Voit, J. Frahm, C. R. Weiss, D. L. Kraitchman, P. A. Bottomley, *BME Front.* **2021**, *2021*, 6185616.
[108] S. Sathyanarayana, M. Schr, D. L. Kraitchman, P. A. Bottomley, *JACC: Cardiovasc. Imaging* **2010**, *3*, 1158.
[109] J. Barrese, X. R. Sun, N. Patel, P. Jethwa, S. F. Danish, *Interdiscip. Neurosurg.: Adv. Tech. Case Manag.* **2014**, *1*, 76.

© 2022 The Authors. Advanced Materials Technologies published by Wiley-VCH GmbH